Electron-impact excitation cross-section measurements at EBITs from 1986 to 2006[1]

Hui Chen and Peter Beiersdorfer

Abstract: This paper reviews the electron-impact excitation (EIE) measurements at electron beam ion trap (EBIT) facilities in the last 20 years. EIE cross sections are important atomic parameters fundamental to understanding the spectroscopic properties of ions. The properties of an EBIT make it an ideal device to measure the EIE cross section of highly charged ions. As a matter of fact, a report of EIE measurement was among the first papers published on the first EBIT ever built, EBIT-I. Since then, a wide range of measurements have been performed for K-shell and L-shell highly charged ions of Ti, V, Cr, Mn, Fe, Xe, and Ba using a combination of crystal spectrometers and solid-state X-ray detectors. In the last few years, the measurements were extended to all strong Fe L-shell lines by using a 6 × 6 pixel array microcalorimeter.

PACS Nos.: 32.30.Jc, 32.30.Rj, 34.50.Fa, 32.70.Cs

Résumé : Nous passons ici en revue les mesures d'excitation par impact électronique (EIE) faites à différents pièges ioniques avec faisceau d'électrons au cours de 20 dernières années. Les sections efficaces EIE constituent d'importants paramètres atomiques, fondamentaux dans le compréhension des propriétés spectroscopiques des ions. Les caractéristiques du piège ionique à faisceau d'électrons en font un appareil idéal pour mesurer les sections efficaces EIE des ions fortement ionisés. De fait, un rapport sur des mesures EIE a fait partie des toutes premières publications faisant état des résultats du premier piège à être construit, EBIT-I. Depuis, beaucoup de mesures ont été faites dans les couches K et L d'ions fortement chargés de Ti, V, Cr, Mn, Fe, Xe et Ba, en utilisant une combinaison de spectromètres à cristaux et de détecteurs état solide pour les rayons-X. Ces dernières années, les mesures ont été étendues à toutes les fortes lignes de la couche L du Fe en utilisant un calorimètre en réseau de 6 × 6 pixels.

[Traduit par la Rédaction]

1. Introduction

Electron impact processes are basic and among the most important atomic processes leading to line emission in a collisional plasma. Measurements of cross sections for various electron impact atomic processes are fundamental both to test atomic theories and calculations, and to understand plasma emission from laboratory and astrophysical plasmas (for more details see refs. 1–5 and the references cited therein.)

Various experimental capabilities have been developed in the past decades to measure the cross sections of direct electron-impact excitation, dielectronic recombination (DR), and radiative recombination (RR) for ions of different Z and different charge states. Until the invention of the electron beam ion trap (EBIT) in 1986, a measurement of the cross section for EIE was possible only for ions with charge $q \leq +6$ by using the then available techniques of crossed or merged beams [6, 7]. EBIT (for details see ref. 8 and the reviews of Marrs [9] and Beiersdorfer [10]) is a device that is ideally suited, and at the present still the only device, for measuring the EIE cross sections of X-ray transitions in highly charged ions. Highly charged ions nowadays are also available from sources other than an EBIT, for example, from electron cyclotron resonance (ECR) ion sources. However, measurements with ions from these sources have so far been limited to those involving optical or UV transitions and electron-impact energies below about 30 eV [11–13]. This is a result of the electron-energy-loss spectroscopy techniques employed in such merged beam measurements. For example, measurements have been performed for ions with charges as high as Fe^{13+}, but only for a transition with energy near 2.4 eV, i.e., of a transition in the visible. Measurements of EIE cross sections with higher electron impact energies besides those carried out on EBITs have so far been limited to neutral systems, such as the measurement of the EIE of neutral helium with energies as high as 500 eV [14].

In the past 20 years, there were numerous papers from EBITs that addressed the issue of electron–ion interaction processes. For example, the DR process was first studied by Knapp et al. [15], while electron impact ionization cross sections were measured by Wong et al. [16]. In this review, we will focus on direct electron impact excitation (DE) cross-section measurements. This catalogue of work is represented by the 11 publications listed in Table 1, all utilizing one of three electron beam ion traps EBIT-I, EBIT-II, and SuperEBIT. These three EBITs have all been situated at the Lawrence Livermore National Laboratory. To our knowledge, EIE cross-section measurements have

Received 22 June 2007. Accepted 13 August 2007. Published on the NRC Research Press Web site at http://cjp.nrc.ca/ on 26 January 2008.

H. Chen[2] and P. Beiersdorfer. High Temperature and Astrophysics Division, Lawrence Livermore National Laboratory, Livermore, CA 94550-9234, USA.

[1] Paper given at the Workshop on Twenty Years of Spectroscopy with EBIT held in Berkeley, California, 13–15 November 2006.

[2] Corresponding author (e-mail: chen33@llnl.gov).

 doi: 10.1139/P07-152 © 2008 NRC Canada

Table 1. List of the EIE cross-section measurements using electron beam ion traps.

Year	Authors	Measured ions	Facility	Journal	Ref.
1988	Marrs et al.	Ne-like Ba	EBIT-I	Phys. Rev. Lett.	17
1992	Chantrenne et al.	He-like Ti	EBIT-I	Phys. Rev. Lett.	18
1995	Wong et al.	Li-like, He-like Ti, V, Cr, Mn and Fe	EBIT-I	Phys. Rev. A	19
1999	Gu et al.	B-like to Li-like Fe	EBIT-II	Astrophys. J.	20
2000	Widmann et al.	He-like and H-like Xe	SuperEBIT	Am. Inst. Phys. Conf. Ser.	21
2001	Gu et al.	B-like to Li-like Fe	EBIT-II	Astrophys. J.	22
2002	Chen et al.	Li-like Fe	EBIT-II	Astrophys. J. Lett.	23
2005	Chen et al.	B-like to Li-like Fe	EBIT-I	Astrophys. J.	24
2005	May et al.	Cu-like and Ni-like Au	EBIT-I	Nucl. Instrum. Methods B	25
2006	Chen et al.	F-like to Li-like Fe	EBIT-I	Astrophys. J.	26
2006	Brown et al.	Ne-like Fe	EBIT-I	Phys. Rev. Lett.	27

not yet been carried out at other EBIT facilities. There is no obvious reason for this other than choice. As will become clear in the following, normalization and assigning a reliable EIE cross section involves a complicated analysis chain, which includes characterizing the response functions of multiple spectrometers and accounting for polarization effects, etc., and therefore requires a dedicated and specialized effort.

The arrangement of this paper is as follows. After a discussion of the basic atomic processes involved in a collisional plasma that contribute to line emission (Sect. 2), we describe, in Sect. 3, the cross-section measurement technique. Section 4 is devoted to the instrument requirements and experimental setups, while Sect. 5 gives special attention to various aspects of the data analysis. Highlights of the experimental results are presented in Sect. 6, followed by a summary in Sect. 7.

2. Atomic processes

In a collisional plasma, mainly three electron-impact atomic processes are active to produce line emission: direct excitation, dielectronic recombination, and resonance excitation.

The direct excitation (DE) process can be described for element A with charge $Z+$ as

$$A^{Z+} + \mathrm{e}^- \rightarrow A^{Z+}(l') + \mathrm{e}^- \rightarrow A^{Z+}(l) + \mathrm{e}^- + h\nu$$

where $l = s, p, d$, etc. This process, illustrated in Fig. 1, dominates the line excitation atomic processes at energies above the EIE threshold.

Below the EIE threshold, an atomic process known as dielectronic recombination (DR) can be very effective in producing line emission. The process is given by

$$A^{Z+} + \mathrm{e}^- \rightarrow A^{(Z-1)+}(l') \rightarrow A^{(Z-1)+}(l) + h\nu$$

DR lines may be distinct from their parent line if the free electron is captured into a level close to that of the ground electron, which is excited in the process, as shown in Fig. 2. But if the free electron is captured into a level with a much higher principal quantum number n, then the resulting DR line has only a slightly lower photon energy than the DE line, and

Fig. 1. Schematic of direct excitation process.

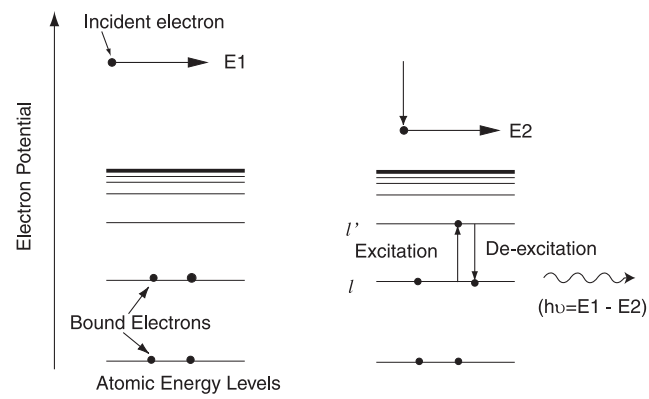

Fig. 2. Schematic of dielectronic recombination process.

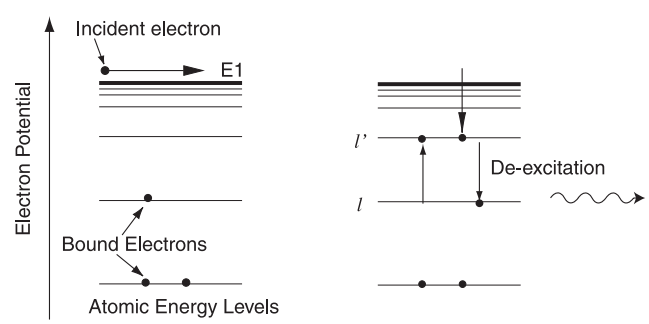

can be distinguished from the DE line only if the spectrometer has very high resolution and the lines are not broadened by any other mechanism. DR onto very high n levels thus produces satellites that typically cannot be resolved from the DE line.

The third process, resonant excitation (RE), occurs above but near the excitation threshold

$$A^{Z+}+\mathrm{e}^- \rightarrow A^{(Z-1)+}(l'') \rightarrow A^{Z+}(l')+\mathrm{e}^- \rightarrow A^{Z+}+\mathrm{e}^-+h\nu$$

RE, illustrated in Fig. 3, can populate the same levels as DE,

© 2008 NRC Canada

Fig. 3. Schematic of resonance excitation process.

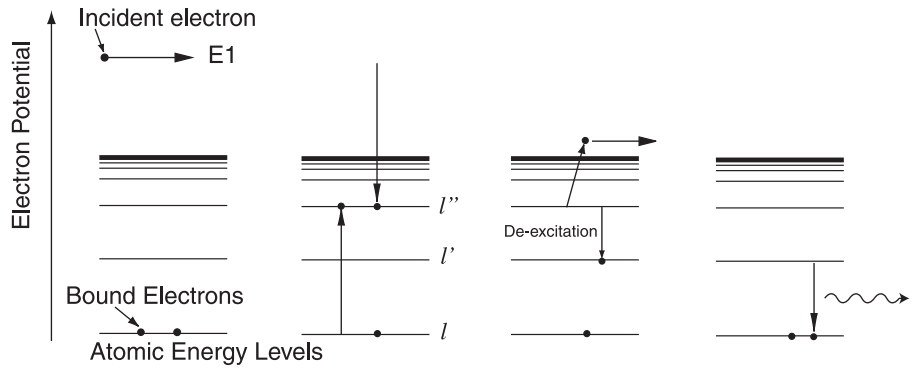

Fig. 4. Photons as a function of electron energy (bottom) and the line-out spectrum (top) from an EBIT-II measurement taken from ref. 20, and reproduced with permission of the American Astronomical Society. The nearly horizontal line on the bottom figure indicates the EIE threshold energy.

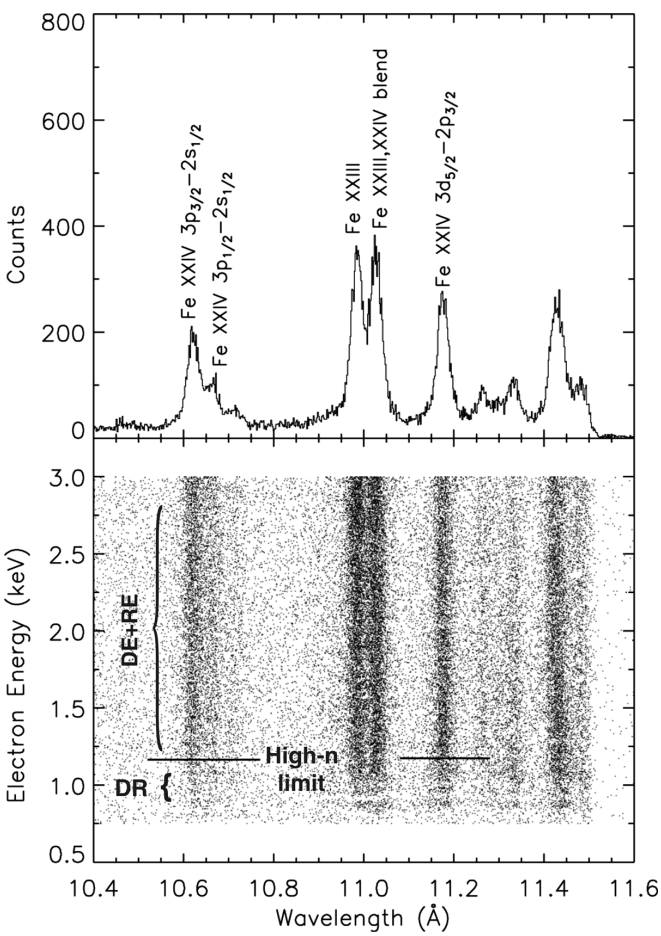

but via dielectronic capture followed by autoionization to the level of interest.

Experimentally, a spectrum from all three processes can be obtained simultaneously, if the photon emission is measured as a function of the exciting electron energy. By selecting the electron-beam energy in an EBIT to be in a certain energy range, it is possible to maximize the contribution from the atomic process of interest. Using this method, DR near the He-like Ni XXVII excitation threshold has been investigated by Knapp et al. [15]. (For additional details on DR measurements on EBITs please see, for example, refs. 28, 29, and references cited therein.) Similarly, Beiersdorfer et al. [30] were able to demonstrate the increase of line emission due to resonance excitation. Figure 4 is an example of a two-dimensional (photon energy versus electron energy) spectrum of Fe XXIV (bottom panel) taken at an EBIT at electron energies ranging between 0.75 and 3 keV [20]. The direct excitation threshold is marked by a (nearly) horizontal line. The two-dimensional spectrum can then be used to make a one-dimensional (line intensity versus photon energy) spectrum (top panel).

Additional atomic excitation processes involved in the line radiation include cascades. This is illustrated in Fig. 5. Cascades can contribute to the upper level population in addition to the direct EIE process. The effect of cascades was noted for the first time on EBIT-I in the line emission of Ba XLV [30], as cascades can form distinct step-like increases in the line emission as the electron energy increases and higher lying levels become accessible. Cascade contributions to the population of these upper levels are illustrated in Fig. 6 for X-ray transitions studied by Marrs et al. [17] in the first EIE cross-section measurement. Because a multitude of upper levels may contribute to the population of a given level, the DE cross sections derived from the observed intensity of a given line at a given electron energy are often called "effective" DE cross sections in papers [19, 23]. Effective DE cross sections thus are the sum of the direct EIE cross section plus all cascade contributions. Cascade contributions can play an important role at above threshold energies — as shown in Fig. 6, they may contribute more than 90% for some lines. This must be taken into account in comparisons of theoretical and experimental cross sections. The progress in computer models of the line emission in recent years make possible more precise predictions of cascade contributions by including higher n levels. For example, $n = 4$ was included in the calculations of Fe XXIV in 2002 [23], while in 2006, cascades from $n = 12$ were calculated [26]. Better accounting of cascade contributions in the theoretical predictions allows for a more meaningful comparison of theoretical predictions to the measurements, which by their nature take into account all possible cascade effects.

© 2008 NRC Canada

Fig. 5. Schematic of cascade contribution to the excited level population.

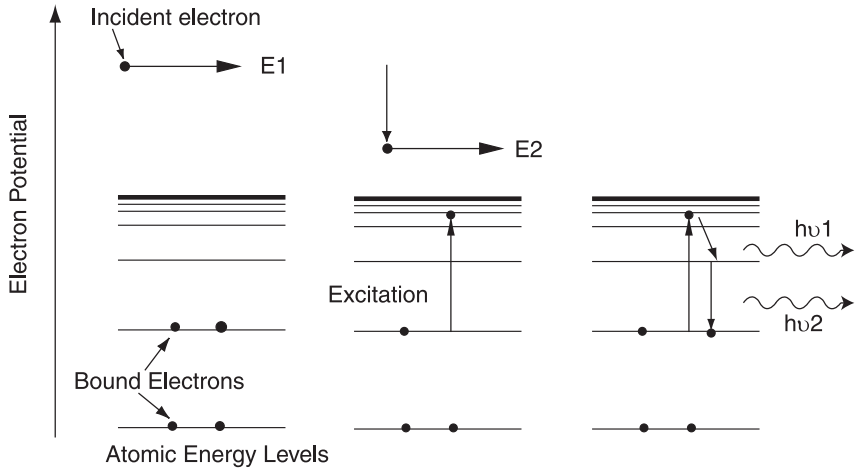

Fig. 6. Cascades and branching decay for Ba^{46+} Reprinted with permission from ref. 17. Copyright 1988 American Physical Society.

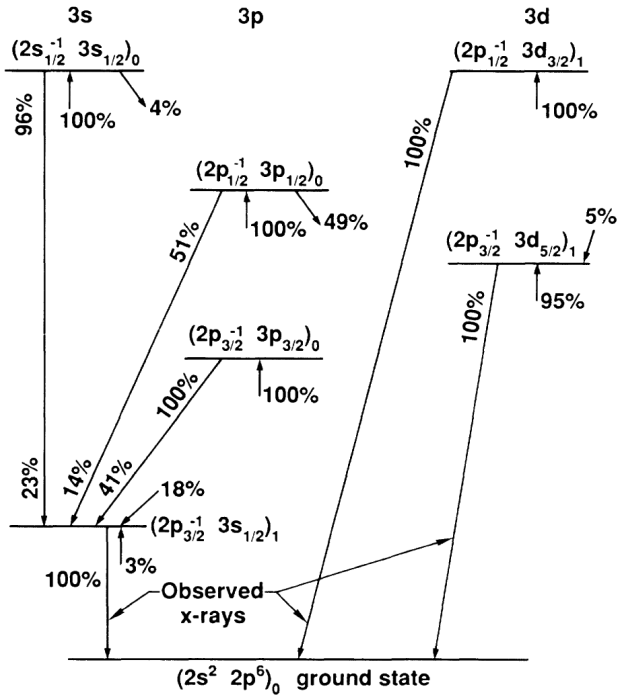

3. EIE cross-section measurement technique on EBITs

In an EBIT, the electron energy can be fairly precisely controlled. This enables a good selection of the desired atomic processes to be measured. The EBIT is also known for its capability to control the charge state of a given element (charge balance). Many factors can affect the charge balance in the trap, including the electron-beam energy, impurities, and ion injection methods. A good charge balance can be achieved by skillfully operating the EBIT with an optimum combination of different controls. A good charge balance is especially important for measuring L- and M-shell ions where lines are crowded (as illustrated by the Fe L-shell line wavelength surveys [31–33]). More precise measurements can be made by limiting possible blending with lines from other, undesired charge states. In a word, the EBIT has been an ideal device to measure EIE cross sections

> because the target ions are prepared in a single charge state and the electron beam is mono-energetic, it is possible to unravel all of the separate cross sections which contribute to X-ray emission [17].

For the Livermore EBITs, the experimental capabilities for measuring the EIE cross sections have progressed over the years. These include diagnostic developments (more in Sect. 4), data analysis (in Sect. 5), and the EBIT device itself. The most obvious progression is the development of a high-energy EBIT. At Livermore, this was accomplished by changing from EBIT-I to SuperEBIT [34], where the electron-beam energy can reach 250 keV, producing the capability of "stripping the uranium atom bare". A less noticeable but important development for the EBITs is the capability of manipulating, at will, the electron-beam energy as a function of time. The simplest form is using a constant electron-beam energy, as used in the first EIE cross-section measurement [17]. Later, Chantrenne et al. [18] and Wong et al. [19] altered beam energies within the same trapping cycle, using the first energy to prepare ions in a desired charge state and then using the second energy to excite them. In the next step, the electron beam was made to sweep linearly between two energies [15, 20] and it was eventually programmed to sweep in such a pattern that the electron population simulated a Maxwellian plasma condition [35] (see the paper by Savin et al. [36] in this issue). Other hardware was developed at the same time, for example, an event-mode data acquisition system [37], to extract data from these complex sweep patterns.

Below, we discuss in more detail the EIE cross-section measurement technique, specifically, we will describe the commonly used technique that employs normalization to the cross sections for nonresonant radiative electron capture.

© 2008 NRC Canada

Formally, the EIE cross section σ is related to the observed line intensity I for a fixed electron impact energy by the equation

$$I^{\mathrm{EIE}} = A\sigma^{\mathrm{EIE}} v \int_V n_{\mathrm{e}} n_{\mathrm{i}}\, \mathrm{d}V \tag{1}$$

where A represents instrumental factors related to such parameters such as observation angle and detection efficiency, σ is the cross section of the line to be measured, and v is the electron impact velocity. n_{e} is the electron density and n_{i} is the ion density. The integral is over the emitting volume V^{EIE} covered by the instrument.

In general, an EIE cross section can be measured either relatively or absolutely. Energy-dependent relative cross sections associated with a given line can be determined by normalizing to a theoretical cross section at one energy value [20]. While this procedure does not produce absolute cross sections, it can produce quite accurate results, if the theoretical cross section is trustworthy, as is the case at high electron impact energies where the Born approximation is valid. Another relative measurement is accomplished by normalizing to the EIE cross section associated with another line. Such measurements use a ratio of (1), $I_a/I_b \approx \sigma_a/\sigma_b$, in which many of the parameters can be eliminated especially if the two lines are close to each other and instrumental factors do not change appreciably. In many cases, this technique simply studies line intensity ratios, for example, in refs. 38 and 39. We will not discuss relative measurements any further in this paper. We focus instead on "absolute" EIE cross-section measurements.

An "absolute" measurement brings the measured EIE cross section to an absolute scale. This is done by normalizing the measurement directly to the radiative recombination (RR) cross sections. RR is chosen for normalization because first, it is currently impossible to measure the absolute number of ions in the trap as well as the electron-beam-ion overlap (i.e., the volume integral) so that no normalization to geometric quantities is possible, and second, as the inverse of photon ionization, RR is the simplest atomic-scattering process and at high-energy involves only one electron and one photon and this is the best known of all theoretically determined cross sections. An RR X-ray is produced by capturing a free electron into a bound level. The X-ray photon has an energy equal to the sum of the energy of the free electron and ionization potential of the level into which the electron is captured. As stated by Chantrenne et al. [18],

> Unlike calculations of electron collision cross sections, those for RR, obtained through detailed balance from photoionization cross sections, do not involve electron correlations and thus can be performed very accurately. Photoionization experiments with atoms confirm the theoretical accuracy to be better than 3%. Calculation for RR for highly charged ions are deemed better.

Normalizing the excitation cross section to that producing RR radiation involving the same target ion has been the basic technique used for all the EIE cross-section measurements reviewed here.

In the RR normalization technique, the intensity of a line produced by EIE, (1), is normalized to that of RR lines from the same charge state measured at the same time

$$I^{\mathrm{RR}} = B\sigma^{\mathrm{RR}} v \int n_{\mathrm{e}} n_{\mathrm{i}}\, \mathrm{d}V^{RR} \tag{2}$$

Similarly to (1), B represents instrumental factors. σ^{RR} is the RR cross section. The integral is over the emitting volume V^{RR}.

From (1) and (2), σ^{EIE} is given by

$$\sigma^{\mathrm{EIE}} = \frac{A}{B}\frac{I^{\mathrm{EIE}}}{I^{\mathrm{RR}}}\sigma^{\mathrm{RR}}\frac{\int n_{\mathrm{e}} n_{\mathrm{i}}\, \mathrm{d}V^{\mathrm{RR}}}{\int n_{\mathrm{e}} n_{\mathrm{i}}\, \mathrm{d}V^{EIE}} \tag{3}$$

In general, the volume of ions excited by electron impact is the same volume of ions emitting radiative recombination photons, and the integral terms cancel, resulting in a very simple expression for σ^{EIE}

$$\sigma^{\mathrm{EIE}} = \frac{A}{B}\frac{I^{\mathrm{EIE}}}{I^{\mathrm{RR}}}\sigma^{\mathrm{RR}} \tag{4}$$

Below we discuss the instrumental requirements an EIE cross-section measurement. Following this discussion, we will discuss in Sect. 5 the instrumental parameters A and B in more detail.

4. Instrumental requirements

To realize the RR normalization technique, it is highly desirable that the spectrometers record the excitation lines as well as the RR lines simultaneously as this minimizes the differences in the instrumental parameters A and B in (3). This requirement calls for three basic qualities of the spectrometer. First, the spectrometer should have a broad spectral coverage because the energy of the EIE emission is less than (or at most equal to) that of the impacting electron, while the RR emission energy is the addition of electron energy and ionization potential and thus higher than the energy of the impacting electron. Second, the spectrometer should have sufficient spectral resolving power to discern both the EIE and RR lines of interest. Third, the instrument throughput should be sufficiently large to allow a measurement to be completed within a reasonable time duration. This is a nontrivial requirement, as σ^{RR} easily is many orders of magnitude smaller than σ^{EIE}, making the detection of RR photons challenging.

So far, a single instrument has not met all of these requirements. Both conventional photon-counting solid-state detectors such as Ge detectors and, more recently, microcalorimeters can meet the first and the third requirements. They have broadband spectral coverage and good throughput. But they have not been able to meet the second requirement: the spectral resolving power of these detectors is not sufficient to resolve the important lines excited by electron impact, although recent developments of microcalorimeters have come very close to this goal and are now resolving the bulk of the EIE lines in carefully chosen experiments. As a result, these instruments have been complemented by crystal spectrometers which, depending

© 2008 NRC Canada

Fig. 7. Fe L-shell spectra taken with the XRS and the crystal spectrometer from ref. 23, reproduced by permission of the American Astronomical Society. The three marked transitions are Li-like Fe lines the Li3 ($3d_{5/2} \rightarrow 2p_{3/2}$), Li5 ($3p_{1/2} \rightarrow 2s_{1/2}$), and Li6 ($3p_{3/2} \rightarrow 2s_{1/2}$).

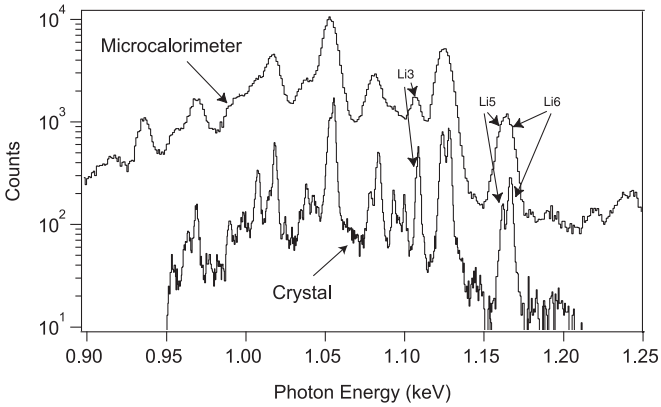

Fig. 8. Instrumental setup for EIE cross-section measurements on the Livermore EBIT-I device.

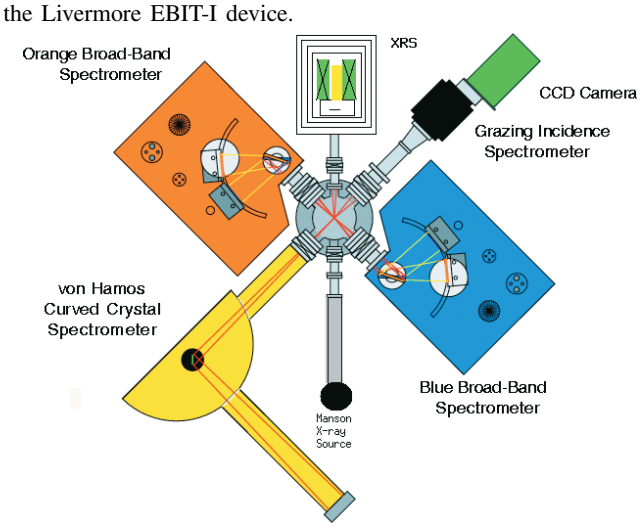

on the crystals and the spectrometer geometry employed, can have resolving powers up to 10 000 within a narrow spectral band width. Figure 7 is an example of a measurement of the Fe L-shell spectrum using the microcalorimeter and a crystal spectrometer.

Combinations of a broadband spectrometer together with a crystal spectrometer have been used for virtually all of the EIE measurements. Historically, before the year 2000, the combination of solid-state detectors (high-purity Ge detector or SiLi detector) with a crystal spectrometer was used in EIE cross-section measurements. After 2000 the XRS microcalorimeter was used in place of conventional solid-state detectors. A typical instrumental setup on EBIT-I is shown in Fig. 8, with two flat-grating spectrometers [40, 41], a von Hámos crystal spectrometer [42], the XRS [43–46], and a broad-band grazing incidence grating spectrometer [47].

The XRS microcalorimeter detector used in Livermore EBIT measurements was made at the NASA Goddard Space Flight

Fig. 9. Comparison of EBIT spectra obtained with a Ge detector and the XRS microcalorimeter. The spectral resolving power of the XRS is about 10 times higher than that of the Ge detector.

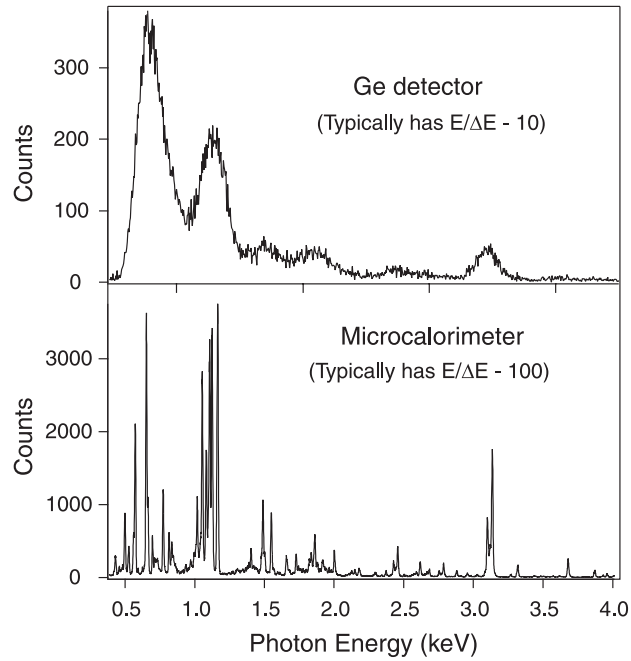

Center [43, 45, 46, 48]. It is the engineering unit from the *Astro-E* space flight mission [49]. It has an energy resolution better than 10 eV and an energy coverage of about 13.5 keV (500 eV to 14 keV). Figure 9 illustrates the improvement of the spectral resolving power of the XRS microcalorimeter over that of a solid detector. The XRS has unique features that enabled the EIE measurements. These are a combination of a highly effective area (12.5 mm^2), electronic stability, and a microsecond time resolution. So far, none of these has been duplicated by calorimeter devices used elsewhere. This combination is particularly important for measuring the cross section of low- and mid-Z ions because the RR cross sections of L-shell iron ions, for example, are about two orders of magnitude smaller than the electron-impact excitation cross sections. In other words, only one RR X-ray is recorded for 100 counts in a given line excited by electron impact. Considering that EBIT devices are inherently not very bright X-ray sources, the microcalorimeter must thus have both a large dynamic range as well as stable electronic gain to allow a long enough observation period to accurately measure the RR spectrum. The technical details and more recent developments of this detector are reviewed by Porter et al. in this issue [46].

Crystal spectrometers employed in cross-section measurements either employed reflective crystals (mostly flat or cylindrically curved) [17–20, 22–24, 26] or transmissive crystals [21]. The resolving power of the spectrometers ranged from many hundreds to a few thousand. When used on an EBIT, a critical feature has to be taken into account during the measurement: the reflectivity of a crystal is dependent on the polarization of the incident light. Induced by the electron-beam, X-ray emission from EBIT is linearly polarized. This brings an extra degree of complexity to the data analysis, as discussed below.

© 2008 NRC Canada

5. Spectral analysis

In practice, several details need to be considered to derive the EIE cross sections from the setup described above. For example, the instrumental factor A (or B) can be expressed as $\alpha G\eta T$, where G represents the effect of polarization on the measurement, η is the quantum efficiency of the detector, and T is the transmission of filters in the system.

Another important factor is the geometrical factor α that determines how much plasma is seen by the spectrometer. This factor mainly plays a role when comparing the line intensities measured by two different instruments. In that case, normalization is made by choosing a line (or several lines) that is observed by both spectrometers. For example, the sum of all He-like lines was selected by Wong et al. [19], while Chen et al. [23] chose the two Fe XXIV lines $1s^2\,3p_{1/2} \rightarrow 1s^2\,2s_{1/2}$ and $1s^2\,3p_{3/2} \rightarrow 1s^2\,2s_{1/2}$ as common references. These reference lines are normally well-isolated from the other lines and their intensities can be determined accurately with each instrument. Furthermore, the intensity of the RR radiation typically needs to be described as a summation over the fine-structure components. As a result, the equation used for data analysis is given by

$$\sigma^{\mathrm{EIE}} = \frac{\alpha^{\mathrm{RR}}}{\alpha^{\mathrm{EIE}}} \frac{\sum_j G_j^{\mathrm{RR}} \eta_j^{\mathrm{RR}} T_j^{\mathrm{RR}}}{G^{\mathrm{EIE}} \eta^{\mathrm{EIE}} T^{EIE}} \frac{I^{\mathrm{EIE}}}{I^{\mathrm{RR}}} \sigma_j^{\mathrm{RR}} \tag{5}$$

where σ^{EIE} is the total cross section for producing the line (which includes cascade contributions. The summation is over the fine-structure components j contributing to the observed intensity I^{RR}.

The detection efficiency η has several parts. For a crystal spectrometer it includes the quantum efficiency of the detector and the crystal reflectivity. The transmission efficiency T must account for all absorption of X-rays between the source and the detector. For example, in the case of a crystal spectrometer using a position-sensitive gas proportional counter, T includes the photon absorption of the gas in the proportional counter in additional to any foils and detector window between EBIT trap and the detector. The efficiency of Ge or SiLi detectors and the microcalorimeter include mostly the detector quantum efficiency η and the transmission efficiency of various foils used for heat shields as well as that of potential ice build-up on the detector. Any change of the detector efficiency during the experiment will affect the final result and therefore should be monitored and accounted for. To monitor for ice build-up on the XRS, for example, an X-ray tube, which was mounted on the opposite port (c.f. Fig. 8), was used on EBIT-I.

5.1. RR cross sections

RR cross sections used for normalization have generally been calculated using a Hartree–Slater model [50, 51]. This was done for photon emission at 90° relative to the in-coming electron and for each level j of the target ion charge state. As mentioned before, the results from such calculations have been tested and found to be in good agreement with photoionization experiments [52]. Since the RR energy is the sum of the level potential (precisely calculated) and the electron-beam energy (precisely set experimentally), the energy of the RR line can be determined from these two quantities. Also, from the cross section, we can determine the relative intensity of the an RR feature within the same charge state: $I^{\mathrm{RR}} \propto n_{\mathrm{i}} \sigma_j^{\mathrm{RR}} v_{\mathrm{e}}$. As a matter of fact, accurate knowledge of the energy (position) and relative intensity (amplitude) of each RR fine-structure components provides tight constraints for fitting the RR line intensity (see the following section), and therefore results in an accurate analysis of the observed RR line intensity.

RR cross sections were calculated and presented mostly on a case-by-case basis for selected electron energies. However, Savin et al. [35] presented the energy dependence of RR cross section of K-shell Ar ions via a multiparameter expression. Similarly, Chen et al. [24] made a fit to the calculated RR cross sections of L-shell Fe ions for electron energies (in keV) ranging between 0.5 and 10 keV using a fifth-order polynomial fit in inverse energy $(1/E)$, i.e., $\sigma = a(1/E)^0 + b(1/E)^1 + c(1/E)^2 + d(1/E)^3 + e(1/E)^4 + f(1/E)^5$. The fitting parameters are listed in Table 2.

5.2. RR line intensity

The accuracy with which the RR intensity can be determined directly affects the accuracy of the measurement of σ^{EIE}, as is easily seen from (5). Depending on the measurement setup, the RR spectrum was either measured by a Ge detector or by the XRS microcalorimeter. Unlike a Maxwellian plasma, RR X-rays excited by a nearly mono-energetic electron beam form distinct, resolved features whose width is determined by the resolving power of the detector, energy distribution of the electron beam, and the spread of the fine-structure components. Often, it is not possible with the broad-band spectrometer to resolve the fine-structure components of a given RR feature associated with a given ion. In fact, in some cases it is not even possible to resolve RR features associated with different charge states. Completely resolving the RR fine-structure components is, however, not necessary. The separation of the RR components and their relative intensities, well-known from theory, provide strict constraints in the spectral fitting of the RR features.

Furthermore, when using the XRS, it is possible to determine the energy spread of the electron beam from the RR spectral width. For example, it was determined that the energy spread of the electron beam was 40 ± 2 eV for a 2.1 keV electron beam, and 44 ± 3 eV for a 3.0 keV beam [23]. This width is larger than the fine-structure separations of the individual RR components. These separations are as small as 10 eV (see Fig. 10 where the individual RR components are indicated by thin lines); consequently, we cannot resolve them in the XRS spectrum despite the $\leq$10 eV resolving power of the microcalorimeter. However, the separations of the RR features among different charge states are typically more than twice the electron-beam energy width and can be distinguished clearly in the XRS spectrum.

Finally, it should be noted that one can also extract the charge balance of the ions in the trap from the RR spectrum

$$n_{\mathrm{i}} \propto \frac{I^{\mathrm{RR}}}{\sum_j G_j^{\mathrm{RR}} \eta_j^{\mathrm{RR}} T_j^{\mathrm{RR}} \sigma_j^{\mathrm{RR}}} \tag{6}$$

This charge balance information can then be used in fitting the spectrum produced by EIE as described later.

© 2008 NRC Canada

Table 2. Energy-dependent cross sections of RR captures (in units of 10^{-24} cm^2) into $n = 2$ fine-structure levels expressed by a six-parameter polynomial from ref. 24, reproduced by permission of the AAS.

			Fitting Parameters					
Ion	Capture level	Ioniz. potential (eV)	a	b	c	d	e	f
Fe XXIV	$2s_{1/2}J = 1/2$	2046	−11.246	256.630	120.343	−134.196	64.849	−11.477
Fe XXIV	$2p_{1/2}J = 1/2$	1997	−1.025	−1.272	342.710	−260.136	102.948	−16.196
Fe XXIV	$2p_{3/2}J = 3/2$	1981	−1.703	−7.414	670.755	−506.274	199.805	−31.397
Fe XXIII	$2s_{1/2}2s_{1/2}J = 0$	1951	−5.590	125.475	59.147	−68.937	33.887	−6.056
Fe XXIII	$2s_{1/2}2p_{1/2}J = 0$	1908	−0.207	−1.101	87.725	−65.667	25.745	−4.025
Fe XXIII	$2s_{1/2}2p_{1/2}J = 1$	1904	−0.607	−3.543	261.808	−195.746	76.675	−11.978
Fe XXIII	$2s_{1/2}2p_{3/2}J = 2$	1892	−0.849	−8.154	428.865	−319.023	124.652	−19.453
Fe XXIII	$2s_{1/2}2p_{3/2}J = 1$	1855	−0.566	−3.959	254.884	−190.871	74.837	−11.698
Fe XXIII	$2p_{1/2}2p_{1/2}J = 0$	1832	−0.023	0.629	0.583	−0.730	0.379	−0.071
Fe XXIII	$2p_{3/2}2p_{3/2}J = 0$	1772	−0.214	5.003	1.967	−2.545	1.296	−0.235
Fe XXII	$2p_{1/2}J = 1/2$	1800	−0.646	−7.564	363.570	−269.323	104.790	−16.295
Fe XXII	$2p_{3/2}J = 3/2$	1785	−0.944	−19.778	711.219	−523.565	203.110	−31.550
Fe XXI	$2p_{1/2}2p_{1/2}J = 0$	1688	−0.279	−3.788	166.241	−124.785	48.871	−7.629
Fe XXI	$2p_{1/2}2p_{3/2}J = 1$	1679	−0.342	−8.123	273.985	−203.701	79.257	−12.314
Fe XXI	$2p_{1/2}2p_{3/2}J = 2$	1674	−0.485	−10.634	367.592	−273.369	106.411	−16.542
Fe XXI	$2p_{3/2}2p_{3/2}J = 2$	1658	−0.119	−2.494	87.312	−65.214	25.463	−3.967
Fe XXI	$2p_{3/2}2p_{3/2}J = 0$	1637	−0.044	−0.325	19.703	−14.752	5.742	−0.890
Fe XX	$2p_{3/2}J = 3/2$	1572	−0.397	−13.749	408.734	−302.912	117.589	−18.246
Fe XX	$2p_{1/2}2p_{3/2}2p_{3/2}J = 3/2$	1554	−0.300	−8.980	277.541	−206.063	79.990	−12.401
Fe XX	$2p_{1/2}2p_{3/2}2p_{3/2}J = 1/2$	1536	−0.058	−0.970	39.130	−29.408	11.482	−1.784
Fe XX	$2p_{3/2}J = 3/2$	1529	−0.003	−0.080	2.653	−1.974	0.771	−0.120
Fe XIX	$2p_{3/2}2p_{3/2}J = 2$	1454	−0.295	−12.756	358.971	−266.294	103.276	−16.008
Fe XIX	$2p_{3/2}2p_{3/2}J = 0$	1444	−0.052	−2.354	64.762	−47.835	18.471	−2.852
Fe XIX	$2p_{1/2}2p_{3/2}(3)J = 1$	1443	−0.084	−4.347	117.896	−87.691	34.083	−5.292
Fe XIX	$2p_{1/2}2p_{3/2}(3)J = 2$	1433	0.000	−0.204	5.128	−3.917	1.555	−0.246
Fe XVIII	$2p_{3/2}J = 3/2$	1352	−0.146	−14.267	346.643	−255.437	98.435	−15.179
Fe XVIII	$2p_{1/2}J = 1/2$	1339	−0.006	−0.679	16.182	−11.960	4.613	−0.711

© 2008 NRC Canada

Fig. 10. An RR spectrum (histogram) and its fit (continuous line) of L-shell Fe taken with the XRS microcalorimeter at an electron-beam energy of 3 keV from ref. 23, reproduced by permission of the American Astronomical Society. The vertical lines topped by open diamonds indicate the position and the relative intensity of the individual RR fine-structure components. The peaks are labeled in the form A–B, where A represents charge state of the ion capturing an electron and B is the charge state after recombination. All capture is into the $n = 2$ shell.

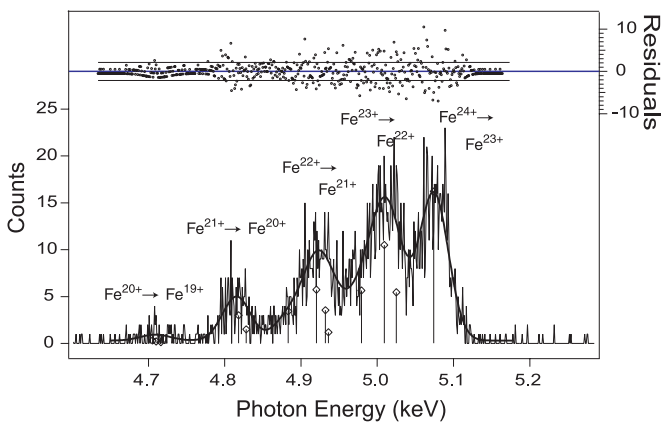

5.3. Effect of polarization

The mono-energetic electron beam in an EBIT excites ions in a preferred direction and this results in linearly polarized X-ray emission. Polarization affects not only the line intensity recorded with instruments that are directly sensitive to polarization, such as crystal spectrometers, but also the emission collected with all instruments that view the trap with a small solid angle and thus at a well-defined angle with regards to the electron beam [53–56]. It was estimated [57] that polarization can affect the inferred cross section by up to 60%. It, therefore, should be taken into account.

So far, all excitation cross-section measurements were made by viewing the ions along a line of sight perpendicular to the electron beam. The line emission I^{90} at 90° relates to the 4π-averaged, isotropic line emission $I^{4\pi}$ through the factor F, i.e., $I^{90} = FI^{4\pi}$. F, in turn, can be expressed in terms of the linear polarization parameter P. For a perfectly mono-directional electron beam, P is defined as $P = (I_\pi - I_\sigma)/(I_\pi + I_\sigma)$, where I_π is the emission polarized parallel to the beam direction, and I_σ is the emission polarized perpendicular to the beam direction. For an electric-dipole (E1) transition [55]

$$F = 3/(3 - P) \tag{7}$$

For a magnetic-dipole (M1) transition

$$F = 3/(3 + P) \tag{8}$$

A more complete treatment of polarization can be found in many publications [54–56, 58–65]. These papers discuss in detail the polarization effects on spectral measurements employing an EBIT source, and these papers and their references provide more information such as the theoretical derivation of (6) and (7), along with the more complex expression for magnetic-quadruple (M2) transitions.

It should be mentioned that there is a depolarizing effect due to a transverse beam energy (typically on the order of 100–200 eV) which has been investigated by Beiersdorfer et al. [55, 66] and Gu et al. [67]. This effect is caused by the spiraling electron beam [66–68] that effectively modifies the polarization parameter. The depolarization effect was taken into account in the EIE cross-section measurements after 1999.

Another aspect of polarization manifests itself in the crystal spectrometer measurement. Crystals inherently reflect the two polarization components differently and thus act as polarizers. The nature of polarization-sensitive crystal reflectivity has also been addressed in several papers [20, 55, 59, 60, 67]. Briefly, two models, perfect crystal and mosaic crystal, can be used to infer the crystal reflectivity [69]. The average value of the two models was commonly used in the data analysis, unless the crystal is known to be perfect.

In the absence of measurements, P was often obtained by calculation using, for example, the code in ref. 70, and more recently, the Flexible Atomic Code (FAC) [71]. In cases where measurements of the polarization were made, these calculations were found to be accurate within the error bars [54–56, 58–61]. An exception was found for the Lyman-α transitions in hydrogen-like ions [60, 65]. In general, we established the calculations to be accurate within 20%. This typically affects the accuracy of EIE cross-section measurements to within only a few percent.

5.4. EIE line intensity

For an EIE spectrum with few, well-resolved lines from the same charge state, spectral fitting can be straight forward: the line intensities can be derived by fitting the lines with either a Gaussian or a Voigt (a convolution of a Lorentzian and Gaussian function) profile. The line width normally is the same for all the lines in the same spectrum.

More often than not, EIE lines from different charge states are present in the same spectral band. Knowledge of the charge balance and line blending is therefore critical in the analysis of the EIE lines. Using oscillator strengths calculated by theory, the charge balance can often be estimated from the intensity ratio of the observed lines from neighboring charge states (for example, the Ba^{45+} satellite emission to the Ba^{46+} parent line was used in ref. 17 to estimate the relative ion abundance). A more precise estimate of the charge balance can be inferred from the RR line intensities as described previously. As a matter of fact, RR lines have been used in most of the EIE papers [17, 19, 23, 24, 26] to infer the charge balance. Knowledge of the charge balance then can be used as a fixed parameter in the spectral fitting model. To best resolve blended lines, we also need both precise wavelengths and the relative line intensities of the blended lines.

For example, to analyze the complicated Fe L-shell spectrum shown in Fig. 11, an empirical model was constructed utilizing the data from an Fe L-shell line survey [32]. The model included all observed L-shell emission lines with measured wavelengths and relative intensities of the lines from all charge states. From

© 2008 NRC Canada

Fig. 11. Fe L-shell EIE spectrum and its fit using an empirical model from ref. 24, reproduced by permission of the American Astronomical Society. The position and intensity of contributing lines are given by the underlying stick plot. Lines are labelled using the notation A*n*, where A represents the charge state and *n* is the line index. For example, Li6 is the line 6 among the L-shell lines observed in Li-like Fe XXIV.

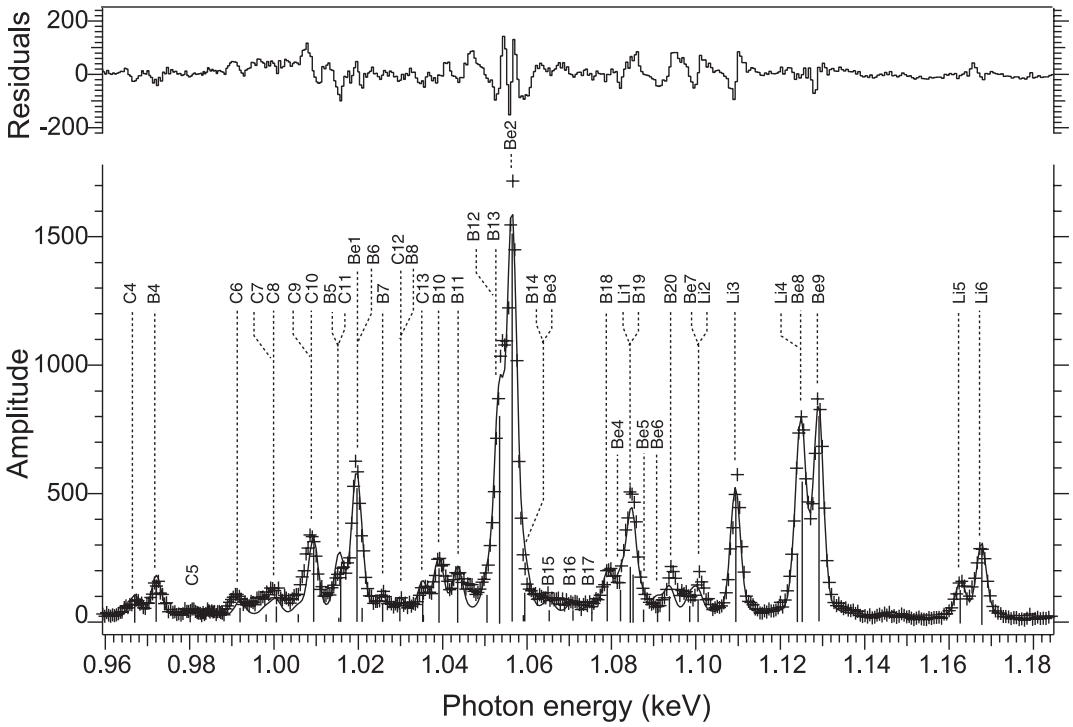

Fig. 12. Fe L-shell RR spectrum from ref. 26, reproduced by permission of the American Astronomical Society. measured with the XRS microcalorimeter (dots with statistical error bars) at an electron-beam energy of 2.93 keV. The peaks are labeled in the form A–B, where A represents charge state of the ion capturing an electron and B is the charge state after recombination. The continuous line is the fit to the measurement using the semi-empirical model described in the text.

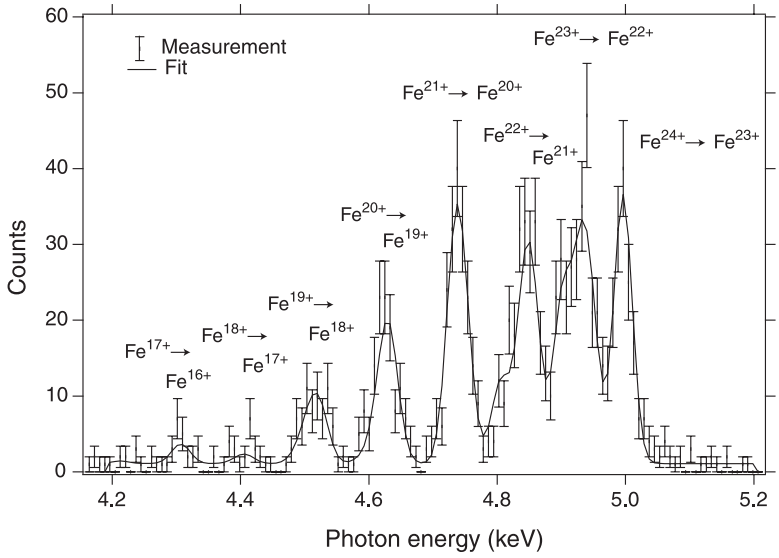

the charge balance obtained fitting the RR emission, we derived initial amplitudes for each line using the available relative intensities of lines from each individual charge state [32]. During fitting, the relative intensity of each line was allowed to vary within 30% to account for unmeasured factors such as polarization effects and intensity changes at different electron-

© 2008 NRC Canada

Fig. 13. Crystal spectrometer spectrum of the Fe L-shell transitions at an electron-beam energy of 2.93 keV. The continuous line is the measurement, and the dotted line is the fitted spectrum using the semi-empirical model from ref. 26, reproduced by permission of the American Astronomical Society. described in the text. Lines are labelled using the notation An, where A represents the charge state and n is the line index. The only exception is the line labeled 5D, which represents the $5d_{5/2} \rightarrow 2p_{3/2}$ transition in Fe XVII.

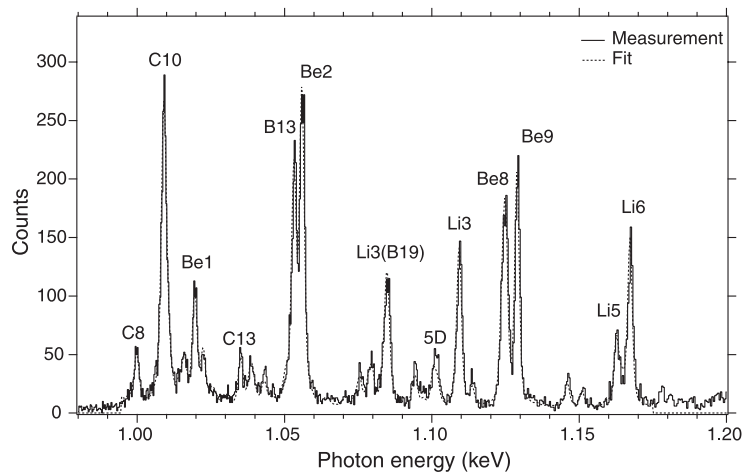

beam energies. The position of the lines, however, remained fixed. This information provided us with a constraint similar to that provided by fitting the RR emission discussed above. As is shown in Fig. 11, we achieved good fits to the measured spectra using this method.

A more sophisticated, semi-empirical model for analyzing complex EIE spectra is demonstrated in ref. 26. Compared to the empirical model described above, this model takes virtually all possible lines into account. Many of these lines are too weak and blended to be measured, and, therefore, could not be included in the empirical model above. The information for this model was based on the atomic data calculated with the FAC Code [71]. It starts with a theoretical data base that includes thousands of lines, most of which were individually very weak but contributed to the spectrum collectively. When comparing the theoretical model with the experimental data, the theoretical cross sections were adjusted for a subset of strong lines to achieve acceptable agreement. This allowed the determination of the measured cross sections for this subset of lines; yet any possible contamination by weak lines in the determination of the intensities of strong lines was accounted for in this analysis. The essential feature of this multistep process was that the line intensities within the same charge state were derived from measurements with a high-resolution crystal spectrometer, while the overall normalization for each charge state was derived from a comparison of $3 \rightarrow 2$ and RR emission recorded with the XRS microcalorimeter. This approach was needed to account for the contribution from thousands of lines from multiple charge states (up to all 8 L-shell ions). Figures 12 and 13 illustrate the goodness of the fit using this method for a radiative recombination spectrum (Fig. 12) and a crystal spectrum (Fig. 13) taken at the same time for an electron energy of $E_b = 2.93$ keV. Both spectra show that the lines from low-charge states such as C-like Fe XXI, and even Ne-like Fe XVII coexist with Li-like Fe XXIV.

5.5. Error analysis

The uncertainty of the resulting cross section is a quadrature summation of the uncertainties from all possible terms in (4). The sum comprises, for example, the counting statistics for individual lines in the crystal data and the RR peak; the uncertainty due to polarization corrections; the uncertainties in the detection efficiency estimate; the uncertainty due to background modeling in both crystal and broad-band spectrometer. This analysis has been applied in virtually every paper reviewed here.

6. Highlights of experimental results

The electron impact excitation cross-section measurements in the past two decades had a diverse focus with regard to the target ions and the experimental details. Generally speaking, we can divide the measurements into two groups. The first corresponds to the use of a solid-state detector in combination with a crystal spectrometer measuring K-shell Ti, V, Cr, Me, Fe, and L-shell ions Ba. One measurement in this group is of He-like Xe using SuperEBIT [21]. Chronologically, this group of papers was published between 1988 to 2000. The second group of papers, published after 1999, is predominantly on the L-shell Fe ions. One exception is a measurement of M-shell Au [25]. This second group compromises measurements using the microcalorimeter instead of solid-state detectors for broad-band spectral coverage. The following highlights the results from both measurement groups.

6.1. EIE cross-sections measurements between 1986–2000

The paper by Marrs et al. [17], which was the first to report measurements with EBIT, presented Ne-like Ba^{46+} EIE cross sections at two electron energies of 5.69 and 8.2 keV. These measurements were made before many of the now common EBIT tools, such as the MeVVA [72] injection system, were available. Ba was chosen because as a constituent of the electron gun, it naturally existed in EBIT. The analysis did not take polarization effects into account, and the theoretical calculation did not include cascades from levels with $n > 3$. This paper, however, demonstrated the powerful new technique afforded by EBIT, and therefore represents as a significant mile-

© 2008 NRC Canada

Table 3. Comparison of measured and theoretical EIE cross sections (in unit of 10^{-21} cm^2) for Ne-like Ba^{46+}. All data are from ref. 17.

Level	Electron energy (keV)	Photon energy (eV)	σ-measured	σ-calculation[a]
Sum $J = 0$	5.69		2.50 ± 0.35	2.60
Sum $J = 0$	8.20		2.27 ± 0.32	1.94
$(2p_{3/2}^{-1}3d_{5/2})_1$	5.69	4937	3.98 ± 0.56	3.56
$(2p_{3/2}^{-1}3d_{5/2})_1$	8.20	4937	3.30 ± 0.46	3.23
$(2p_{1/2}^{-1}3d_{3/2})_1$	5.69	5295	2.12 ± 0.30	2.00
$(2p_{1/2}^{-1}3d_{3/2})_1$	8.20	5295	1.82 ± 0.25	1.82

[a]Relativistic distorted-wave calculation for Ba^{46+}, ref. 73.

Fig. 14. Measured Ti^{20+} EIE cross sections, from ref. 18, as a function of electron energy and the comparison with a fully relativistic distorted-wave calculation. Reprinted with permission from ref. 18. Copyright 1992 American Physical Society.

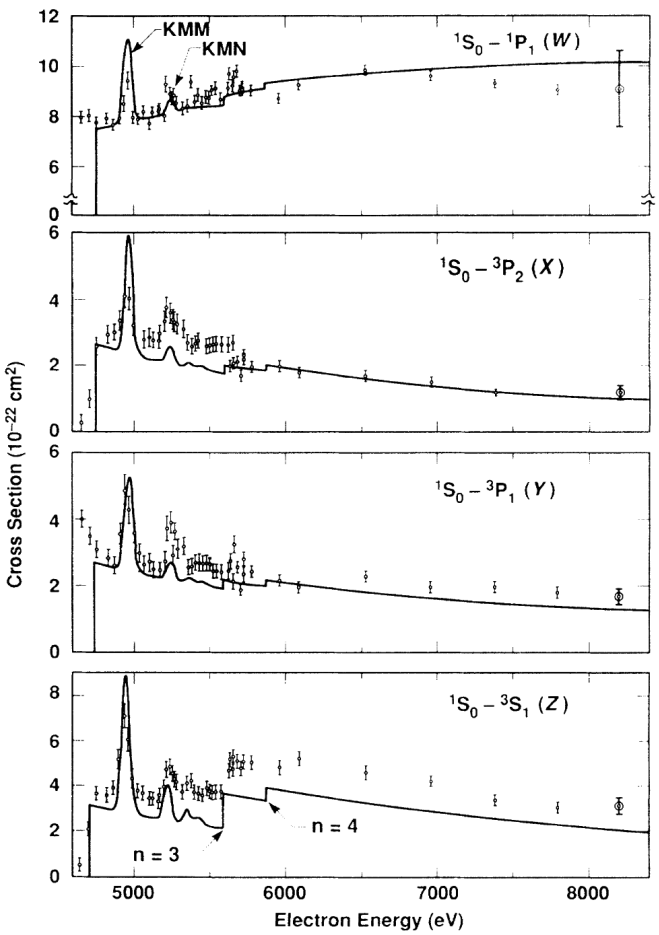

stone. EIE cross sections at two beam energies were reported for three lines, $2p_{1/2}3d_{3/2}$ to $2s^22p^6$, $2p_{3/2}3d_{5/2}$ to $2s^22p^6$, and $2p_{3/2}3s_{1/2}$ to $2s^22p^6$. The results were compared with calculations utilizing the Coulomb–Born-exchange method as well as with a fully relativistic distorted-wave method, as shown in Table 3.

The second milestone in EIE measurements followed a few years later. Chantrenne et al. reported in 1992 the first EIE cross-section measurements as a function of electron energy. Their measurement, which concentrated on He-like Ti^{20+} ions, flipped between two electron-beam energies within the EBIT trapping cycle; the first one was to make the He-like Ti ions, and the second was to excite the ions. Polarization effects were taken into account for the first time in the spectral analysis. The cross-section measurements included not only the contribution from DE, including cascades, but also contribution from resonance excitation, as shown in Fig. 14. Resonance excitation was found to more than double the effective cross section responsible for producing the $n = 2 \rightarrow n = 1$ intercombination and forbidden lines measured. Cascades from $n = 3$ and higher principal quantum number also were found to enhance the effective cross sections by marked amounts. The measurements were compared with DE calculation by a fully relativistic distorted wave code by Zhang et al. [74] augmented by radiative cascades and by results from resonance excitation calculation. Good, though not perfect, agreement was found. Especially the forbidden line z showed notable differences between experiment and calculation. Another important advance made in this paper was that cross sections were extended to high electron energies, which made the derivation of rate coefficients possible. Compared to two theories, it was demonstrated that resonance excitation was important to the overall rate coefficient because it could cause a factor of two difference in the plasma temperature inferred from measured line ratios. The resonance line w and the intercombination line y both demonstrated flux below threshold for excitation, as seen in Fig. 14. The flux below threshold stems from dielectronic satellite transition that have a spectator electron in a very high-n level and, as $n \rightarrow \infty$, map onto their helium-like parent lines in a continuous fashion as shown by Knapp et al. [15] and Beiersdorfer et al. [75].

A subsequent paper on EIE measurements was by Wong et al. [19]. It reported on multiple ions: He-like and Li-like Ti, V, Cr, Mn, and Fe. A technique was presented to manipulate the charge balance between Li-like and He-like ions in the trap. For example, to enhance the Li-like ion population the electron-beam energy was briefly set to the KLL dielectronic resonances for helium-like ions. The electron energy was then switched to the energy at which the spectrum needed for the EIE measurements was taken. In the analysis, proper determination of the charge balance was crucial, and this issue was treated thoroughly. The measured DE cross sections agreed well for all ions with distorted-wave calculations that including radiative cascade contributions. An interesting result from this paper

© 2008 NRC Canada

Fig. 15. EIE cross sections for various He-like ions and the comparison with a distorted-wave calculation (continuous line). Reprinted with permission from ref. 19. Copyright 1995 American Physical Society.

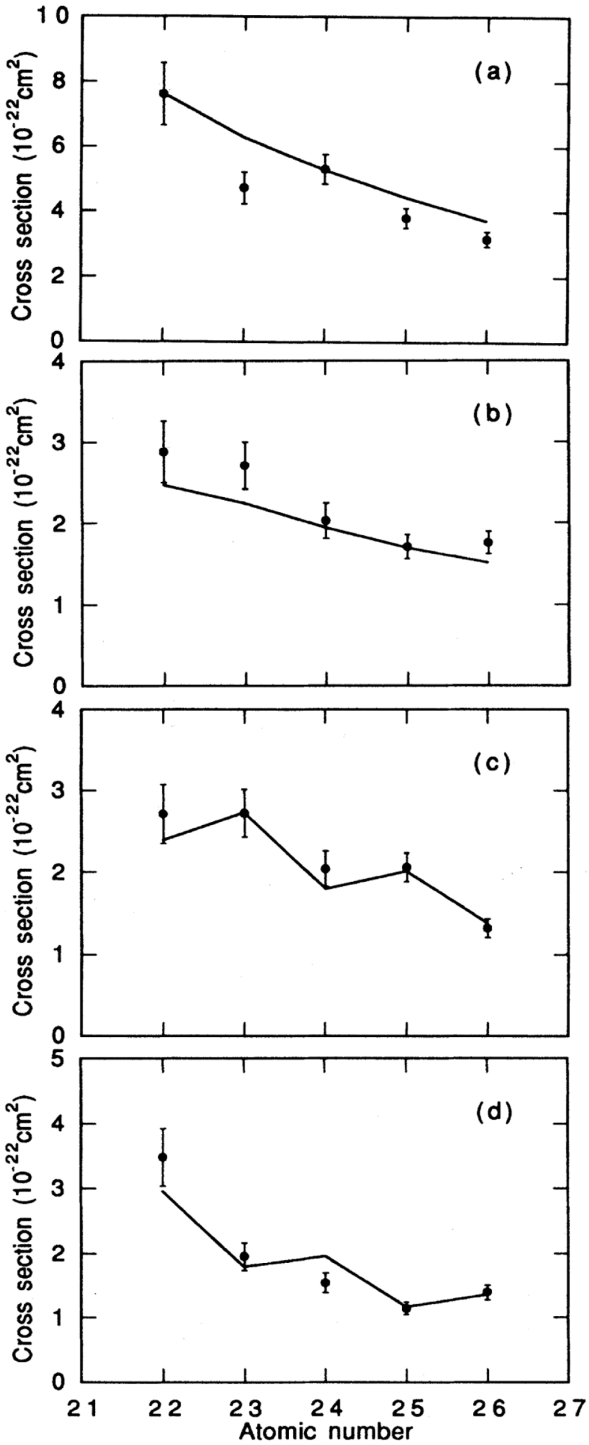

was a demonstration of the effect of the hyperfine interaction in the odd-Z elements V and Mn on the line emission due to a rearrangement of the radiative decay channel of the $^3P_0$ level, which manifested itself as an enhancement of line y at the expense of line z, as illustrated in Fig. 15.

EIE cross sections for high-Z ions were first measured by

Fig. 16. DE and RR spectra of highly charged Xe ions measured with a Ge detector at an electron energy of 112 keV. Spectrum (*a*) was taken within 1 h, and (*b*) was taken over several days. Reprinted with permission from ref. 21. Copyright 2000 American Institute of Physics.

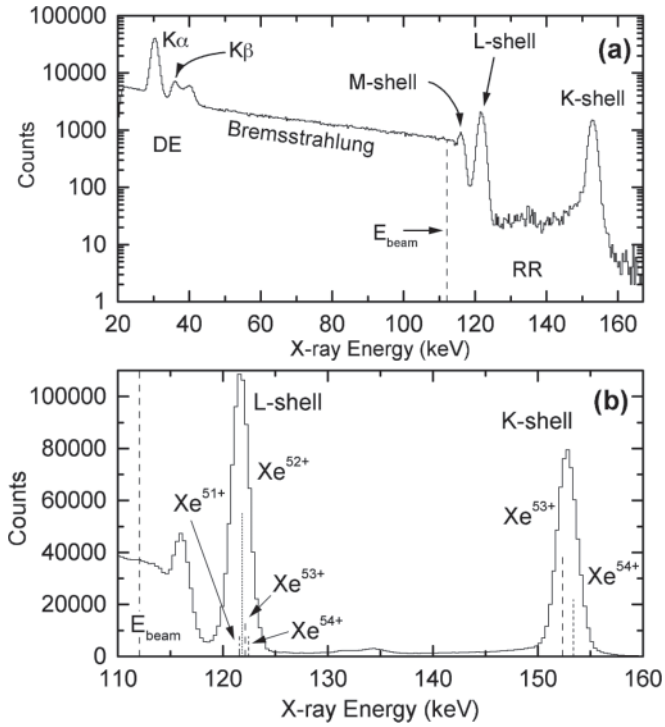

Widmann et al. [21]. Their measurements were performed on SuperEBIT [34] at electron-beam energies of 112 keV. Although the basic technique of the measurement was the same as used before, there were many new technical details that needed to be addressed. For example, the He-like Xe^{52+} Kα excitation lines have energies of about 30 keV, while the corresponding RR lines are at about 122 keV for a 112 keV electron beam. To detect X-rays at these energies, position sensitive proportional counters used for X-rays at much lower energies are no longer sufficiently efficient. Similarly, the resolving power of crystal spectrometers in a typical Johann or von Hámos geometry is no longer adequate due to the small Bragg angle required. Widmann et al. addressed those issues by using a combination of a high-purity Ge detector and a transmission-type crystal spectrometer [76]. Figure 16 shows the He-like Xe spectrum reported by these authors and obtained with the Ge detector. The derived experimental cross sections agreed well with relativistic distorted-wave calculations as long as the Breit interaction was included. This was the first experimental demonstration of this effect, and it clearly shows up for the resonance line w and the intercombination line y, where inclusion of the generalized Breit interaction changes the results by a factor of two. This is illustrated in Table 4.

6.2. EIE cross-section measurements after 1999: the Fe L-shell era

Since 1999, the focus of EBIT EIE cross-section measurements has been on the iron L-shell emission lines [20, 22–24,

© 2008 NRC Canada

Table 4. Comparison between measured σ_{expt} and calculated EIE cross sections for H-like Xe $^{53+}$ and He-like Xe $^{52+}$ ions at an electron energy of 112 keV. The calculated values are based on a distorted-wave approach without (σ_{rel}) and with inclusion of the generalized Breit interaction (σ_{GBI}). All data are from ref. 21.

Line	σ_{expt} (barn)	σ_{rel} (barn)	σ_{GBI} (barn)
$Ly_{\alpha 1}$	8.6 ± 1.5	8.256	8.109
$Ly_{\alpha 2,3}$	8.2 ± 3.4	6.541	6.787
w	7.0 ± 2.0	17.45	8.364
y	3.9 ± 1.5	7.313	3.842

26, 27] as part of the Livermore EBIT laboratory X-ray astrophysics program [5]. This change was correlated with the launch of the XMM-Newton and Chandra X-ray observatories. The primary aim of these two satellites has been to measure the cosmically abundant, spectrally rich L-shell iron ions using the high-resolution instruments on board. Besides measurements of a complete set of Fe L-shell emission line wavelengths [31–33], cross sections have been measured for virtually all strong Fe L-shell lines [20, 22–24, 26, 27].

The first Fe L-shell EIE cross-section measurements were reported by Gu et al. [20, 22]. These measurements focused on the L-shell lines of C-like Fe XXI through Li-like Fe XXIV. They were relative in the sense that the cross sections were normalized to calculations in the high-energy limit where cross-section calculations are normally considered to have the least uncertainty. By sweeping the electron-beam energy across the excitation threshold, Gu et al. made a detailed study of the line formation by all three atomic processes (DE, below threshold DR, and above threshold RE). The study revealed that RE as well as below threshold DR, which are often ignored in spectral calculations, are important in the actual line formation. Similar to the work done by Chantrenne et al. [18], Gu et al. extracted the rate coefficients from the cross sections measured over a wide range of electron energies. These two papers contained new analysis details that were also employed in later measurements, such as taking into account depolarization. Example measurement results are shown in Fig. 17.

Although by normalizing EIE cross section to calculations at higher energies can be fairly reliable, the accuracy of electron-scattering calculations is limited to 15–30% [77], and may be much worse, if the levels are affected by configuration interaction. The true test of theory, therefore, is to bring a given EIE cross section to an absolute scale by normalizing it to an RR cross section. While this procedure had already been successfully demonstrated for K-shell and L-shell transitions of mid-Z and high-Z ions, respectively, it could not be readily applied to the L-shell transitions of iron. The reason was that the available solid-state detectors could not resolve the different RR feature that emanate from the various L-shell iron ions, as they are separated by merely 100 eV. These measurements were made possible thanks to the availability of the XRS microcalorimeter. The first of the absolute Fe L-shell cross-section measurements was performed by Chen et al. [23] for three energies well above the threshold. The result of this work benchmarked the relative measurements by Gu et al. [20, 22], as illustrated in Fig. 17.

Fig. 17. EIE cross sections for three Fe XXIV lines as a function of energy [20, 23]. The continuous lines are the R-matrix calculations of DE and RE augmented by HULLAC [78] calculations for $n \leq 7$ cascade contributions. The dotted lines are the distorted wave calculations plus HULLAC calculations for cascades. The broken lines are HULLAC [78] calculations. Solid circles are the experimental results normalized to the theoretical values of the $3d_{5/2} \rightarrow 2p_{3/2}$ transition at resonance-free energies. Below threshold, line emission is due to DR satellites for electron captured into $n \geq 5$ Rydberg levels. This emission was not included in the calculations. The open circles are the absolute measurements from ref. 23.

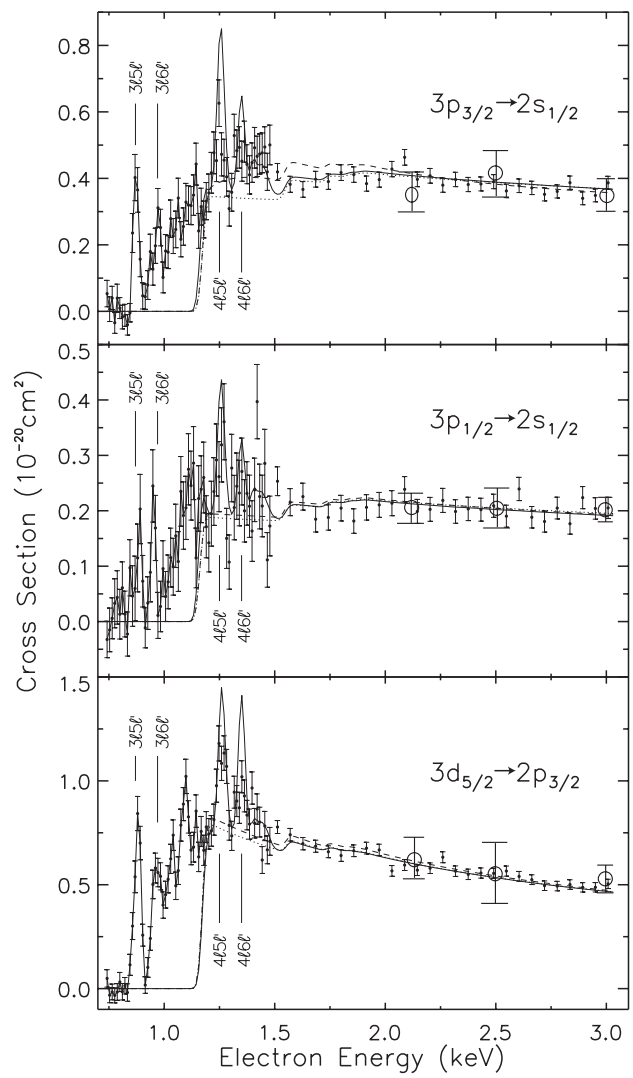

In subsequent papers [24, 26], the EIE cross sections for all strong $3 \rightarrow 2$ lines of F-like Fe XVIII through Li-like Fe XXIV (48 in total) were measured on EBIT-I for multiple electron-beam energies. The empirical [24] and semi-empirical [26] analysis methods discussed above were used to analyze the complex spectra.

Although in most cases the Fe L-shell measurements compare well with calculations, some interesting discrepancies were observed. For example, the effective EIE cross section measured

© 2008 NRC Canada

Fig. 18. Measured effective cross sections (filled circles with error bars) [26] for two C-like Fe lines. Theoretical calculations in the zero-density limit using HULLAC and FAC are shown as a broken line and a continuous line, respectively. Also plotted are measurements from ref. 24 (open circles with error bars). The difference between the two sets of measurements for line C10 is attributed to density effects, as discussed in the text.

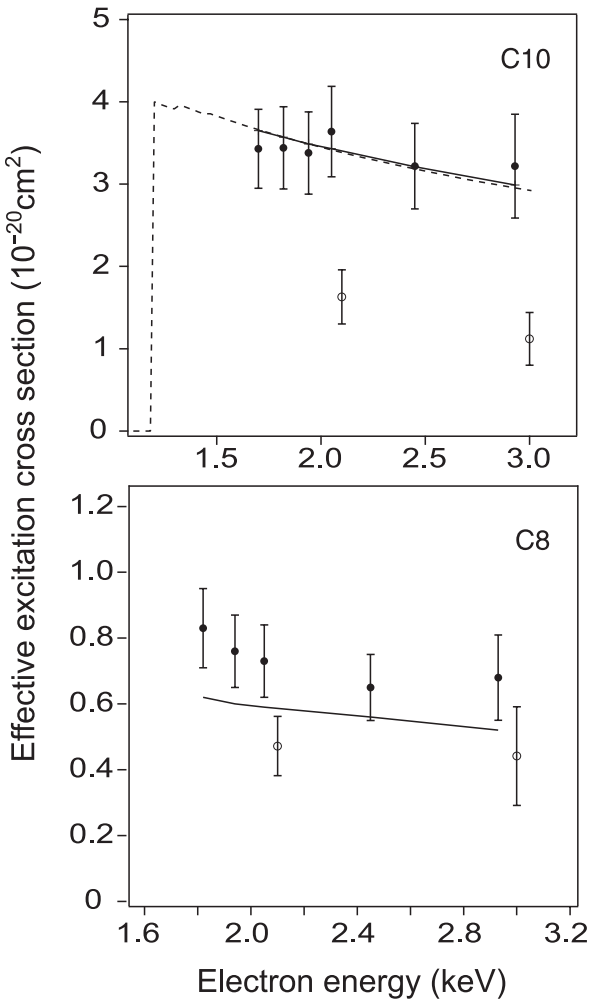

for the C-like Fe line C10 in ref. 24 was about half the value measured later [26]. This is illustrated in Fig. 18. The difference was mostly likely caused by a physical property of this line, namely, its sensitivity to the electron density. This C-like line is among several lines that are sensitive to the electron density due to collisional changes in the population of the $n = 2$ fine-structure levels [79–81]. Calculations showed that the effective excitation cross section changes as a function of electron density for several Fe L-shell lines, as shown in Fig. 19 C10 is the most density-sensitive line of them all.

Further development of the instrumental techniques enabled measurements of the EIE cross sections of the Ne-like Fe XVII lines [27]. The relevant RR features are produced by capture into $n = 3$ levels and thus are even more difficult to resolve than the RR features produced by capture into the $n = 2$ levels of open L-shell iron ions. Moreover, the RR cross sections are yet so small that only one RR photon is observed for roughly 10^3 photons in the EIE lines. These technical issues were resolved with the use of the second-generation X-ray microcalorimeter on EBIT-I. Details of these measurements, which address fundamental problems in solar and X-ray astrophysics are discussed by Brown in this issue [82]. This measurement, in principle, opens up the possibility for determining the EIE cross sections of other systems that require a long counting time (and thus instrumental stability) as well as good resolving power to discern the needed, weak RR features from those of neighboring ions or potential features from background ions.

Fig. 19. Effective theoretical excitation cross sections for some density-sensitive Fe L-shell lines. From ref. 26 and reproduced by permission of the American Astronomical Society

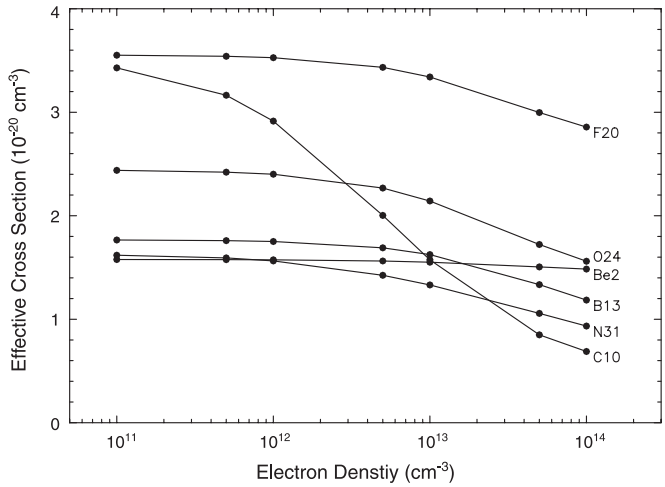

Finally, we mention advances made in measuring EIE cross sections of M-shell transition of gold ions of interest to laser plasma physics. Using the XRS microcalorimeter, May et al. [25] measured of the cross sections for the $3d \rightarrow 5f$ excitations in Cu-like Au^{50+}. Details are discussed in this issue [83].

7. Summary

Much progress was made in the past 20 years to measure EIE cross sections of highly charged ions. Instrumental developments enabled continuous advances in measurement capability extending now to measurements of the cross sections of the $3 \rightarrow 2$ transitions of Fe XVII, which necessitated detecting the weak M-shell RR features. The EBIT technique results in reliable measurements that are unequalled by any other method. The EIE cross-section data have been measured for a wide range of ions and under varied excitation conditions. It has also been demonstrated that rate coefficients can be derived from the EBIT EIE measurements. Good overall agreement has been found between measurements and theory. However, differences on the order of 10–30%, i.e., 2–5 times the measurement accuracy are common, pointing to the need for more accurate theoretical approaches in predicting excitation cross sections.

So far, all EIE measurements have involved X-ray lines. This is because we have chosen the RR process for normalization, and RR features have energies above that of the electron beam and thus are situated in the X-ray regime. Cross-section mea-

© 2008 NRC Canada

surements of lines in the EUV or optical will require a new approach. Such measurements thus represent a challenging new frontier, and we expect that methods will be developed to make advances in these wavelength bands soon.

Acknowledgement

The work at University of California Lawrence Livermore National Laboratory was performed under the auspices of the Department of Energy under Contract No. W-7405-Eng-48. This work was in part supported by the NASA Astronomy and Physics Research and Analysis program under contract NNG06WF081.

References

1. G.H. Dunn. Nucl. Fusion Special Suppl. **2**, 25 (1992).
2. H. Suno and T. Kato. At. Data Nucl. Data Tables, **92**, 407 (2006).
3. A. Dalgarno. *In* Physics of ion–ion and electron–ion collisions. *Edited by* F. Brouillard and J.W. McGowan. Plenum Press, New York. 1983. p. 1.
4. F.B.S. Paerels and S.M. Kahn. Astron. Astrophys. Rev. **41**, 291 (2003).
5. P. Beiersdorfer. Annual Rev. Astron. Astrophys. **41**, 343 (2003).
6. D. Gregory, G.H. Dunn, R.A. Phaneuf, and D.H. Crandall. Phys. Rev. A, **20**, 410 (1979).
7. P.F. Dittner, S. Datz, P.D. Miller, P.L. Pepmiller, and C.M. Fou. Phys. Rev. A, **35**, 3668 (1987).
8. M. Levine, R. Marrs, D. Knapp, and M. Schneider. Phys. Scr. **T22**, 157 (1988).
9. R. Marrs. Can. J. Phys. **85**, (2007). This issue.
10. P. Beiersdorfer. Can. J. Phys. **85**, (2007). This issue.
11. S.J. Smith, A. Chutjian, J.B. Greenwood, and S.S. Tayal. Astrophys. J. **541**, 501 (2000).
12. S.J. Smith, N. Djurić, J.A. Lozano, K.A. Berrington, and A. Chutjian. Astrophys. J. **630**, 1213 (2005).
13. S. Hossain, S.S. Tayal, S.J. Smith, J.C. Raymond, and A. Chutjian. Phys. Rev. A, **75**, 022709 (2007).
14. T.Y. Suzuki, H. Suzuki, F.J. Currell, S. Ohtani, Y. Sakai, T. Takayanagi, and K. Wakiya. Phys. Rev. A, **57**, 1832 (1998).
15. D.A. Knapp, R.E. Marrs, M.A. Levine, C.L. Bennett, and M.H. Chen. Phys. Rev. Lett. **62**, 2104 (1989).
16. K.L. Wong, P. Beiersdorfer, M.H. Chen, R.E. Marrs, K.J. Reed, J.H. Scofield, D.A. Vogel, and R. Zasadzinski. Phys. Rev. A, **48**, 2850 (1993).
17. R. Marrs, M. Levine, D. Knapp, and J. Henderson. Phys. Rev. Lett. **60**, 1715 (1988).
18. S. Chantrenne, P. Beiersdorfer, R. Cauble, and M. Schneider. Phys. Rev. Lett. **69**, 265 (1992).
19. K. Wong, P. Beiersdorfer, K. Reed, and D. Vogel. Phys. Rev. A, **51**, 1214 (1995).
20. M.F. Gu, S.M. Kahn, D.W. Savin, E. Behar, P. Beiersdorfer, G.V. Brown, D.A. Liedahl, and K.J. Reed. Astrophys. J. **518**, 1002 (1999).
21. K. Widmann, P. Beiersdorfer, G.V. Brown, J.R.C. López-Urrutia, A.L. Osterheld, K.J. Reed, J.H. Scofield, and S.B. Utter. Am. Inst. Phys. Conf. Ser. **506**, 444 (2000).
22. M.F. Gu, S.M. Kahn, D.W. Savin, E. Behar, P. Beiersdorfer, G.V. Brown, D.A. Liedahl, and K.J. Reed. Astrophys. J. **563**, 462 (2001).
23. H. Chen, P. Beiersdorfer, G.V. Brown, K.C. Gendreau, K.R. Boyce, R.L. Kelley, F.S. Porter, C.K. Stahle, A.E. Szymkowiak, S.M. Kahn, and J. Scofield. Astrophys. J. Lett. **567**, L169 (2002).
24. H. Chen, P. Beiersdorfer, J.H. Scofield, G.V. Brown, K.R. Boyce, R.L. Kelley, C.A. Kilbourne, F.S. Porter, M.F. Gu, and S.M. Kahn. Astrophys. J. **618**, 1086 (2005).
25. M.J. May, P. Beiersdorfer, N. Jordan, J.H. Scofield, K.J. Reed, S.B. Hansen, K.B. Fournier, M.F. Gu, G.V. Brown, F.S. Porter, R. Kelley, C.A. Kilbourne, and K.R. Boyce. Nucl. Instrum. Methods Phys. Res. B, **235**, 231 (2005).
26. H. Chen, M.F. Gu, P. Beiersdorfer, K.R. Boyce, G.V. Brown, S.M. Kahn, R.L. Kelley, C.A. Kilbourne, F.S. Porter, and J.H. Scofield. Astrophys. J. **646**, 653 (2006).
27. G.V. Brown, P. Beiersdorfer, K.R. Boyce, H. Chen, R.L. Kelley, C.A. Kilbourne, F.S. Porter, A.E. Szymkowiak, M.F. Gu, and S.M. Kahn. Phys. Rev. Lett. **96**, 253201 (2006).
28. D.R. DeWitt, D. Schneider, M.W. Clark, M.H. Chen, and D. Church. Phys. Rev. A, **44**, 7185 (1991).
29. A.J. Smith, P. Beiersdorfer, K. Widmann, M.H. Chen, and J.H. Scofield. Phys. Rev. A, **62**, 052717 (2000).
30. P. Beiersdorfer, A. Osterheld, M. Chen, J. Henderson, D. Knapp, M. Levine, R. Marrs, K. Reed, M. Schneider, and D. Vogel. Phys. Rev. Lett. **65**, 1995 (1990).
31. G.V. Brown, P. Beiersdorfer, S.M. Kahn, D.A. Liedahl, and K. Widmann. Astrophys. J. **502**, 1015 (1998).
32. G.V. Brown, P. Beiersdorfer, D.A. Liedahl, K. Widmann, and S.M. Kahn, and E.J. Clothiaux. Astrophys. J. Suppl. **140**, 589 (2002).
33. H. Chen, M.F. Gu, E. Behar, G.V. Brown, S.M. Kahn, and P. Beiersdorfer. Astrophys. J. Suppl. **168**, 319 (2007).
34. D. Knapp, R. Marrs, S. Elliott, E. Magee, and R. Zasadzinski. Nucl. Instrum. Methods A, **334**, 305 (1993).
35. D.W. Savin, P. Beiersdorfer, S.M. Kahn, B. Beck, G.V. Brown, M.F. Gu, D.A. Liedahl, and J.H. Scofield. Rev. Sci. Instrum. **71**, 3362 (2000).
36. D.W. Savin. Can. J. Phys. **85** (2007). This issue.
37. P. Beiersdorfer, G.V. Brown, L. Hildebrandt, K.L. Wong, and R. Ali. Rev. Sci. Instrum. **72**, 508 (2001).
38. D.W. Savin, P. Beiersdorfer, J.C. López-Urritia, V. Decaux, E.M. Gullikson, S.M. Kahn, D.A. Liedahl, K.J. Reed, and K. Widmann. Astrophys. J. **470**, L73 (1996).
39. G.V. Brown, P. Beiersdorfer, H. Chen, M.H. Chen, and K.J. Reed. Astrophys. J. Lett. **557**, L75 (2001).
40. P. Beiersdorfer and B. Wargelin. Rev. Sci. Instrum. **65**, 13 (1994).
41. G.V. Brown, P. Beiersdorfer, and K. Widmann. Rev. Sci. Instrum. **70**, 280 (1999).
42. P. Beiersdorfer, R. Marrs, J. Henderson, D. Knapp, M. Levine, D. Platt, M. Schneider, D. Vogel, and K. Wong. Rev. Sci. Instrum. **61**, 2338 (1990).
43. F.S. Porter, P. Beiersdorfer, K.R. Boyce, G.V. Brown, H. Chen, R.L. Kelley, and C.A. Kilbourne. Rev. Sci. Instrum. **75**, 3772 (2004).
44. F.S. Porter, M.D. Audley, R.P. Brekosky, R.J. Derro, M.J. Dipirro, K.C. Gendreau, J.D. Gygax, R.L. Kelley, D. McCammon, A. Morell, S.D. Murphy, R.J. Paulos, T. Pham, C.K. Stahle, A.E. Szymkowiak, and J.G. Tuttle. SPIE, **3765**, 729 (1999).

© 2008 NRC Canada

45. F.S. Porter, P. Beiersdorfer, K.R. Boyce, G.V. Brown, H. Chen, K.C. Gendreau, J. Gygax, S.M. Kahn, R.L. Kelley, D.A. Liedahl, C.K. Stahl, A.E. Szymkowiak, and K. Widmann. *In* New century of X-ray astronomy. *Edited by* H. Inoue and H. Kuneida. ASP Conf. Ser. No. 251. Astronomical Society of the Pacific, San Francisco, Calif. 2001. pp. 184–187.
46. F.S. Porter. Can. J. Phys. **85**, (2007). This issue.
47. P. Beiersdorfer, E.W. Magee, E. Träbert, H. Chen, J.K. Lepson, M.F. Gu, and M. Schmidt. Rev. Sci. Instrum. **75**, 3723 (2004).
48. R.L. Kelley, M.D. Audley, K.R. Boyce, S.R. Breon, R. Fujimoto, K.C. Gendreau, S.S. Holt, Y. Ishisaki, D. McCammon, T. Mihara, K. Mitsuda, S.H. Moseley, D.B. Mott, F.S. Porter, C.K. Stahle, and A.E. Szymkowiak. SPIE, **3765**, 114 (1999).
49. Y. Ogawara. *In* The hot universe. Proceedings of IAU Symposium No. 188. *Edited by* K. Koyama, S. Kitamoto, and M. Itoh. Kluwer Academic, Dordrecht, Netherlands. 1998. p. 75.
50. J.H. Scofield. Phys. Rev. A, **40**(6), 3054 (1989).
51. J.H. Scofield. Phys. Rev. A, **44**, 139 (1991).
52. E. Saloman, J. Hubell, and J. Scofield. At. Data Nucl. Data Tables, **38**, 1 (1988).
53. P. Beiersdorfer, T.W. Phillips, K.L. Wong, R.E. Marrs, and D.A. Vogel. Phys. Rev. A, **46**, 3812 (1992).
54. J.R. Henderson, P. Beiersdorfer, C.L. Bennett, S. Chantrenne, D.A. Knapp, R.E. Marrs, M.B. Schneider, K.L. Wong, G.A. Doschek, J.F. Seely, C.M. Brown, R.E. Lavilla, J. Dubau, and M.A. Levine. Phys. Rev. Lett. **65**, 705 (1990).
55. P. Beiersdorfer, D. Vogel, K. Reed, V. Decaux, J. Scofield, and K. Widmann. Phys. Rev. A, **53**, 3974 (1996).
56. P. Beiersdorfer and T. Fujimoto. *In* Proceedings of the 3rd US–Japan Workshop on Plasma Polarization Spectroscopy. 18–21 June 2001. Livermore, Calif. *Edited by* P. Beiersdorfer and T. Fujimoto. University of California, Lawrence Livermore National Laboratory Report No. UCRL-ID-146907. UC-LLNL, Livermore, 2002.
57. H. Chen. *In* Proceedings of the 3rd US–Japan Workshop on Plasma Polarization Spectroscopy. 18–21 June 2001. Livermore, Calif. *Edited by* P. Beiersdorfer and T. Fujimoto. University of California, Lawrence Livermore National Laboratory Report No. UCRL-ID-146907. UC-LLNL, Livermore, 2002.
58. P. Beiersdorfer, J.C. López-Urrutia, V. Decaux, P. Neill, and K. Widmann. Rev. Sci. Instrum. **68**(1), 1073 (1997).
59. D.L. Robbins, A.Y. Faenov, T.A. Pikuz, H. Chen, P. Beiersdorfer, M.J. May, J. Dunn, K.J. Reed, and A.J. Smith. Phys. Rev. A, **70**, 022715 (2004).
60. D.L. Robbins, P. Beiersdorfer, A.Y. Faenov, T.A. Pikuz, D.B. Thorn, H. Chen, K.J. Reed, A.J. Smith, K.R. Boyce, G.V. Brown, R.L. Kelley, C.A. Kilbourne, and F.S. Porter. Phys. Rev. A, **74**, 022713 (2006).
61. P. Beiersdorfer, G. Brown, S. Utter, P. Neill, K.J. Reed, A.J. Smith, and R.S. Thoe. Phys. Rev. A, **60**, 4156 (1999).
62. E. Takács, E.S. Meyer, J.D. Gillaspy, J.R. Roberts, C.T. Chantler, L.T. Hudson, R.D. Deslattes, C.M. Brown, J.M. Laming, J. Dubau, and M.K. Inal. Phys. Rev. A, **54**, 1342 (1996).
63. A.S. Shlyaptseva, S.B. Hansen, V.L. Kantsyrev, B.S. Bauer, D.A. Fedin, N. Ouart, S.A. Kazantsev, A.G. Petrashen, and U.I. Safronova. Rev. Sci. Instrum. **72**, 1241 (2001).
64. A.S. Shlyaptseva, V.L. Kantsyrev, N.D. Ouart, D.A. Fedin, S. Hamasha, and S.B. Hansen. *In* Laser-Generated and Other Laboratory X-ray and EUV Sources, Optics, and Applications. *Edited by* G.A. Kyrala, J.-C.J. Gauthier, C.A. MacDonald, and A.M. Khounsary. Proc. SPIE, **5196**, 16 (2004).
65. N. Nakamura, D. Kato, N. Miura, T. Nakahara, and S. Ohtani. Phys. Rev. A, **63**, 024501 (2001).
66. P. Beiersdorfer and M. Slater. Phys. Rev. E, **64**, 066408 (2001).
67. M.F. Gu, D.W. Savin, and P. Beiersdorfer. J. Phys. B, **32**, 5371 (1999).
68. D.W. Savin, M.F. Gu, and P. Beiersdorfer. *In* Proceedings of the US–Japan Workshop on Plasma Polarization Spectroscopy. 26–29 January 1998. Kyoto, Japan. *Edited by* T. Fujimoto and P. Beiersdorfer. NIFS Proc. Ser. No. 37. National Institute for Fusion Studies, Gifu-ken, Japan. 1998. pp. 90–102.
69. B.L. Henke, E.M. Gullikson, and J.C. Davis. At. Data Nucl. Data Tables, **54**, 181 (1993).
70. H.L. Zhang, D. Sampson, and R. Clark. Phys. Rev. A, **41**(1), 198 (1990).
71. M.F. Gu. Astrophys. J. **582**, 1241 (2003).
72. I. Brown, J. Galvin, R. MacGill, and R. Wright. Appl. Phys. Lett. **49**(16), 1019 (1986).
73. K.J. Reed. Phys. Rev. A, **37**, 1791 (1988).
74. H. Zhang and D. Sampson. Phys. Rev. A, **42**(9), 5378 (1990).
75. P. Beiersdorfer, S. Chantrenne, M. Chen, R. Marrs, D. Vogel, K. Wong, and R. Zasadzinski. Z. Phys. D, **21**, 209 (1991).
76. K. Widmann, P. Beiersdorfer, G. Brown, J.C.L. Urrutia, V. Decaux, and D. Savin. Rev. Sci. Instrum. **68**(1), 1087 (1997).
77. H.L. Zhang and D.H. Sampson. At. Data Nucl. Data Tables, **43**, 1 (1989).
78. A. Bar-Shalom, M. Klapisch, and J. Oreg. J. Quant. Spectrosc. Radiat. Transfer, **71**, 169 (2001).
79. B.J. Wargelin, P. Beiersdorfer, D.A. Liedahl, S.M. Kahn, and S.V. Goeler. Astrophys. J. **496**, 1031 (1998).
80. V. Decaux, V.L. Jacobs, P. Beiersdorfer, D.A. Liedahl, and S.M. Kahn. Phys. Rev. A, **68**, 012509 (2003).
81. H. Chen, P. Beiersdorfer, L.A. Heeter, D.A. Liedahl, K.L. Naranio-Rivera, E. Trabert, M.F. Gu, and J.K. Lepson. Astrophys. J. **611**, 598 (2004).
82. G.V. Brown. Can. J. Phys. **85**, (2007). This issue.
83. M.J. May. Can. J. Phys. **85**, (2007). This issue.

© 2008 NRC Canada